Enabling Multi-electron Reactions in NASICON Positive Electrodes for Aqueous Zinc-Metal Batteries

Kaidi Wang, Huihua Li, Gaoli Guo, Leilei Zheng, Stefano Passerini,* and Huang Zhang*

ABSTRACT: Sodium superionic conductor (NASICON)-structured compounds with a robust polyanionic framework, e.g., $Na_3V_2(PO_4)_3$, have been considered as promising cathode candidates for rechargeable batteries due to their open 3D structure and high thermal stability. However, their practical implementation in aqueous batteries is hindered by their structural instability during the charge/discharge process. Herein, $Na_3V_{2-x}Cr_x(PO_4)_3$ is investigated as a cathode material for aqueous zinc-metal batteries. It is identified that the Cr substitution has a significant effect on improving its rate capability and cycling stability. As a result, the optimal $Na_3V_{1.5}Cr_{0.5}(PO_4)_3$ electrode delivers an ultra-stable cycling performance (68% capacity retention after 10,000 cycles at 1000 mA g^{-1}). A two-electron reaction mechanism between V^{4+}/V^{3+} and V^{5+}/V^{4+} redox couples has been revealed during the electrochemical process for Zn-ion storage. This work verifies the feasibility of multi-electron reactions in NASICON-type cathodes for aqueous zinc batteries and sheds light on designing advanced cathode materials for other aqueous batteries.

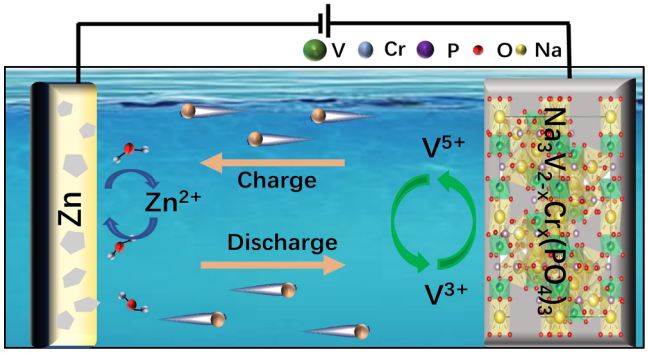

The ever-growing integration of renewable energy sources has boosted the development of low-cost, safe, and efficient energy storage technologies.[1,2] Battery chemistry, inspired by the commercialized lithium-ion batteries (LIBs) for portable electronics and electric vehicles, is also showing promise for grid-scale energy storage.[3] However, because lithium is a limited resource with gradual price increases, the large-scale implementation of LIBs is questionable in view of safety and cost issues.[4] Recently, rechargeable aqueous batteries have been revisited as one of the most promising and feasible candidates for large-scale energy storage applications, favorable for their intrinsic safety and low manufacturing cost from the use of water-based electrolytes.[5,6] Benefiting from the high theoretical capacity (820 mAh g^{-1}) and moderate redox potential (−0.78 V vs standard hydrogen electrode) of the zinc anode, aqueous zinc-metal batteries (AZBs) are attracting particular interest, although tremendous efforts are still in demand to achieve competitive performance for practical applications.[7,8] As key components in batteries, cathode materials play a critical role in determining the performance of AZBs. To date, various types of materials have been investigated as cathodes for AZBs, such as vanadium-based oxides[9,10] and manganese-based oxides.[11,12]

Sodium superionic conductor (NASICON)-structured compounds, having a general formula of $A_xMM'(XO_4)_3$ (A = Li, Na, K; M or M′ = Fe, V, Ti, Cr, Mn; X = S, P, Si, As) and a robust polyanionic framework, have been regarded as promising electrode materials for batteries.[13−15] The open-framework structure not only constructs the 3D Na^+ diffusion pathway but also restricts lattice volume variations during Na^+ extraction/insertion, which is responsible for the decent rate capability and cycling stability. Besides, the strong inductive effect and covalent bonds from the polyanionic groups (e.g., PO_4^{3-}) allow a higher working potential, consequently contributing to the increased energy density and high safety of NASICON cathodes.[16,17] Unfortunately, albeit significant progress has been made, it remains a great challenge to stabilize the capacity of these polyanionic materials in aqueous batteries, often due to their incompatibility with conventional aqueous electrolytes.[18] For example, a typical NASICON

compound, $Na_3V_2(PO_4)_3$ (NVP), has been investigated as a cathode material for aqueous sodium batteries, but it suffers from severe structural degradation.[19,20] NVP materials have also been tested as cathodes in AZBs, and it has been found that they can simultaneously (de)intercalate Zn^{2+}/Na^+ ions from the aqueous electrolyte.[21−23] However, the problem of material dissolution upon either Zn^{2+} or Na^+ insertion/extraction still exists in the AZB configuration, inducing the inevitable capacity decay. In this context, electrolyte engineering appears to be one of the most efficient strategies, making it possible to build robust cathode−electrolyte interphases to prevent the structural deterioration of the NASICON cathode and enable Zn^{2+} transport upon repeated cation insertion and extraction processes.[24−26] For example, our previous work has already demonstrated an efficient electrolyte engineering strategy that involved coupling a crowding agent and mixed cations to stabilize the NVP in AZBs, resulting from the inhibited water activity and anion-involved interphase chemistry.[27] In addition, the substitution of transition metal ions presents another intrinsic route to improve the performance; for example, partial substitution of V by chromium,[28] iron,[29,30] manganese,[31] or aluminum[32,33] has been utilized to enhance the electrochemical performance of sodium-ion batteries. Particularly, V and Mn elements are simultaneously incorporated into the NASICON structure to make use of the electrochemical redox reactions in V and Mn transition metal elements for aqueous Zn-ion storage.[34] Significant increases in energy density and cycle performance have been observed after Mn substitution into NVP to form $Na_4VMn(PO_4)_3$. Transition metal ion substitution in the polyanionic structure can inhibit material dissolution, thus contributing to prolonged cycling stability of NASICON cathodes in AZBs.

Considering the benefit in the fact that NASICON-type electrode materials possess stable frameworks to host cations, it is of great importance to improve the specific capacity, offering higher energy density. NVP materials show the potential of two V^{3+}/V^{4+} and V^{4+}/V^{5+} redox couples, and it has been reported that the proper amount of transition metal substitution into the VO_6 octahedra can activate the V^{4+}/V^{5+} redox couple at high voltage in non-aqueous electrolytes, resulting in remarkably improved energy density. For example, the homogeneous incorporation of Cr^{3+} to V^{3+} not only reinforces the structural stability but also increases the average working potential by triggering the V^{4+}/V^{5+} redox pair in the wide voltage range of 2.5−4.1 V (vs Na/Na^+) during the sodiation/desodiation process.[35] However, to the best of our knowledge, there are still no studies on the multi-electron reaction of NVP-based materials in an aqueous Zn-metal battery, which can be essential and important to boost the energy density of aqueous Zn batteries with NASICON electrodes.

In this work, we investigated the NASICON-type $Na_3V_{2-x}Cr_x(PO_4)_3$ cathodes, which can fully activate the two-electron reaction of vanadium in aqueous zinc-metal batteries. Significantly improved high-rate capacity and long-term cycling stability are achieved, benefiting from the incorporation of Cr^{3+} into the NASCION structure. Particularly, $Na_3V_{1.5}Cr_{0.5}(PO_4)_3$ offers a high reversible capacity of 84.4 mAh g^{-1} at 1000 mA g^{-1} with retention of 68% after extra-long cycling up to 10,000 cycles. Moreover, by employing advanced characterization techniques, the unique two-phase solid−solution reactions are identified which can stabilize the structure upon cation (de)intercalation. This finding provides an unprecedented insight into the development of advanced NASCION-based cathodes for AZBs that can be applied to other types of aqueous batteries for achieving high energy and long lifespan.

The $Na_3V_{2-x}Cr_x(PO_4)_3$ (x = 0, 0.5, 1) compounds were synthesized by a conventional solid-sate method (see experimental details in the Supporting Information) and are denoted as NVP, NVCP-0.5, and NVCP-1.0, according to the specific amount (x) of Cr substituted. Figure S1 shows the powder X-ray diffraction patterns of NVP, NVCP-0.5, and NVCP-1.0 with their Rietveld refinement results. The typical $Na_3V_2(PO_4)_3$ structure (ICSD-114269) and the $Na_3V_{1.5}Cr_{0.5}(PO_4)_3$ structure (ICSD-114268) were used as the structural models for the refinement. To simplify the refinement, the atom positions and occupancies were fixed as in the standard structures (except for the V and Cr occupancies in NVCP-0.5). The cell parameters, scale factor, 10 terms of background fitting, unit cell parameters, and isotropic thermal parameters (U_{iso}) for all atoms were refined. The refinement exhibits satisfactory agreement factors, R_{wp} (weighed residual factor), R_p (Bragg factor), and χ^2, and good weighted profile R factor values (R_{wp} = 7.87, 5.26, and 7.91, respectively) can be obtained. All the observed peaks can be indexed to the standard pattern of a typical NASICON-structured NVP material with a rhombohedral $R\bar{3}c$ space group. The lattice parameters of the $Na_3V_{2-x}Cr_x(PO_4)_3$ phases are summarized in Table S1. Due to the smaller ionic radius of Cr^{3+} (0.615 Å) than that of V^{3+} (0.64 Å), the a, b, and c values gradually decrease as the incorporated Cr^{3+} concentration increases from 0.5 to 1.0, inducing the contraction of the unit cell volume. No other impurity phases were detected, confirming the successful synthesis of the $Na_3V_{2-x}Cr_x(PO_4)_3$ compounds with high phase purity. The occupancies, thermal parameters (U_{iso}), and detailed crystallographic data of NVP, NVCP-0.5, and NVCP-1.0 from the Rietveld refinement are provided in Tables S2, S3, and S4. The crystal structure of $Na_3V_{2-x}Cr_x(PO_4)_3$ (Figure S2) demonstrates the typical open three-dimensional (3D) polyanionic framework, which is built up from isolated VO_6 (or CrO_6) octahedra and PO_4 tetrahedral units interlinked via corners to establish the framework anion $[V_2(PO_4)_3]^{3-}$.[36] Two independent sodium atoms are located in the voids/channels of the framework with two different oxygen environments, i.e., sixfold coordination for the first and eightfold for the second Na^+ cations.[37,38] The doped Cr atoms are randomly distributed in the original V−O octahedral sites. Thermogravimetric analyses (TGAs) for NVCP-0.5 and NVP are shown in Figure S3, and the carbon contents are determined to be 16.5% for NVCP-0.5 and 2.2% for NVP. It should be noted that the introduction of Cr-based raw materials during the synthesis will reduce the consumption of carbon for V reduction, which significantly affects the carbon content in the composites. A nitrogen adsorption/desorption experiment was conducted to investigate the porous structure, as shown in Figure S4. The NVCP-0.5 composite has a specific surface area of 18.534 m^2 g^{-1} based on the Brunauer−Emmett−Teller (BET) method, with its average pore size being around 10 nm.

The surface chemical composition of the NVP, NVCP-0.5, and NVCP-1.0 materials was analyzed by X-ray photoelectron spectroscopy (XPS). The high-resolution V 2p and Cr 2p spectra of NVP, NVCP-0.5, and NVCP-1.0 powders are displayed in Figure S5. The main peaks of V 2p in NVP are located at 515.5 and 522.6 eV, which can be ascribed to the V $2p_{3/2}$ and V $2p_{1/2}$ orbitals of V^{3+}, respectively.[39] The high-

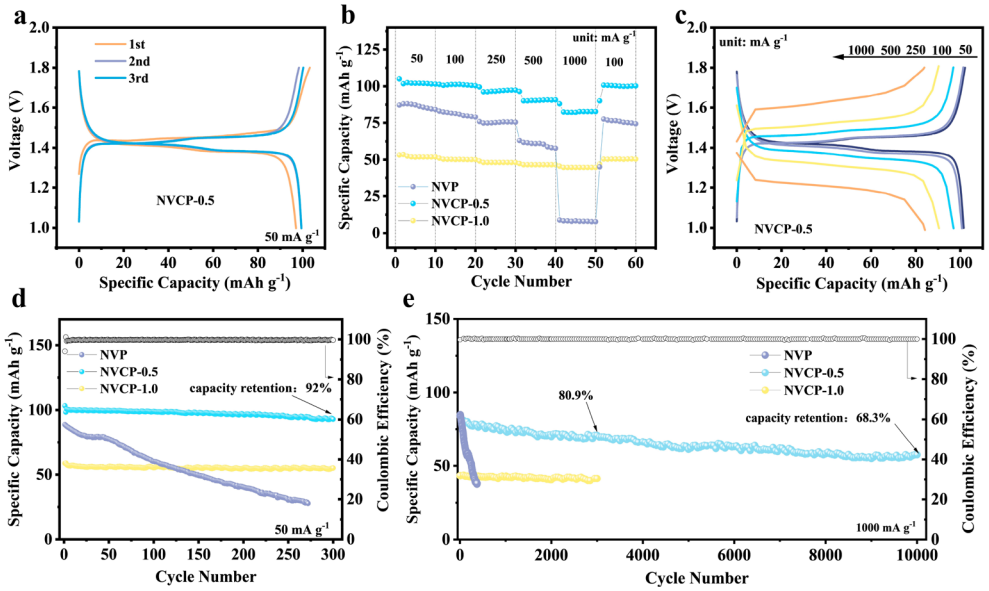

Figure 1. Electrochemical performance of the NVP, NVCP-0.5, and NVCP-1.0 electrodes. (a) Selected charge/discharge profiles of NVCP-0.5 at 50 mA g^{-1} (1st, 2nd, and 3rd). (b) Galvanostatic discharge/charge profiles of NVCP-0.5 at different current densities, ranging from 50 to 1000 mA g^{-1}, for selected cycles. (c) Rate performance of NVP, NVCP-0.5, and NVCP-1.0 at various current densities, ranging from 50 to 1000 mA g^{-1}. (d) Cycling performance of NVP, NVCP-0.5, and NVCP-1.0 at 50 mA g^{-1} for 300 cycles. (e) Long-term cycling performance of NVP, NVCP-0.5, and NVCP-1.0 at 1000 mA g^{-1}. All the specific capacities are based on the mass of the composite including carbon.

resolution Cr 2p spectra of NVCP-0.5 and NVCP-1.0 show two distinct peaks located at 577.1 and 586.6 eV, indicating the presence of Cr^{3+}.[40] When the Cr^{3+} was introduced into the NVP structure, the V valence state was not changed. In addition, the full XPS survey in Figure S6 clearly demonstrates all the identified elements in NVCP, and the atomic concentrations from XPS, listed in Table S5, are close to the theoretical values. Moreover, inductively coupled plasma optical emission spectroscopy (ICP-OES) tests were carried out to analyze the compositions of the NVP and NVCP-0.5 samples. The results are displayed in Table S6. As can be seen, the weight ratio of V to Cr in NVCP-0.5 is ~3.06, corresponding to an atomic ratio of ~3.12, which is slightly higher than the theoretical value of 3. In this context, we used the Cr/V occupancies of 0.24/0.76 and 0.25/0.75 in NVCP-0.5 for the refinement. As presented in Table S3, when the occupancies of V and Cr were fixed at 0.24/0.76, better agreement factors were reached during the refinement. Therefore, the occupancy ratio of V to Cr is calculated to be ~3.17, in good correspondence to the ICP-OES results.

Scanning electron microscopy (SEM), scanning transmission electron microscopy (STEM), and high-resolution transmission electron microscopy (HR-TEM) were used to characterize the morphology and structure of NVP, NVCP-0.5, and NVCP-1.0. The SEM images in Figure S7 reveal that all samples exhibit a typically porous structure, while the overall morphology is strongly affected by the introduction of Cr^{3+}. NVP and NVCP-0.5 present identifiable particles on the surface, while the NVCP-1.0 sample has a foam-like structure, which can be attributed to the increased carbon content in the composite. The microstructure of NVCP-0.5 was further characterized by TEM. The low-magnification TEM image in Figure S8a demonstrates the particle with a width of several hundred nanometers, contracting the porous structure. At higher magnification (Figure S8b), the carbon layer can be distinguished in an average thickness of 4 nm. Lattice fringes with *d*-spacing of 0.369 nm along the particle edge are observed, corresponding to the (113) plane in the rhombohedral NVCP-0.5 phase. Additionally, the energy-dispersive X-ray spectroscopy (EDX) elemental mapping of the discharged electrodes in STEM mode (STEM-EDX) results (Figure S9) clearly demonstrates the uniform elemental distribution of Na, V, Cr, and O in NVCP-0.5.

The electrochemical performances of the $Na_3V_{2-x}Cr_x(PO_4)_3$ materials as cathodes for AZBs were investigated in 2032-type coin cells using zinc foil as anode and 2 *m* $ZnOTF_2$ + 1 *m* NaOTF as electrolyte. The Na salt additive has been reported to be a critical factor affecting the reversibility of both the NASICON-based cathode and the zinc metal.[27,41,42] The initial galvanostatic charge/discharge (GCD) voltage profiles of the NVP, NVCP-0.5, and NVCP-1.0 electrodes were recorded at 50 mA g^{-1} in the voltage range of 1.0−1.8 V and are displayed in Figure S10 and Figure 1a. The NVP electrode delivers a charge capacity of 92.1 mAh g^{-1} and discharge capacity of 87.2 mAh g^{-1} with an initial Coulombic efficiency (CE) of 94.7%. The flat voltage plateau reflects the quasi-one-stage intercalation process.[27,43] When the Cr^{3+} was introduced into the structure, both Cr-doped NVCP-0.5 and NVCP-1.0 electrodes exhibited a new plateau at a higher working voltage. Specifically, the NVCP-0.5 cathode possesses a high reversible capacity of ~100 mAh g^{-1} and an average output voltage of 1.4 V, which are higher than those of NVP. It should be noted that the theoretical capacity of the NVCP-0.5 material is calculated to be 88 mAh g^{-1} if only the V^{3+}/V^{4+} redox couple is considered. In such a case, the achieved capacity of NVCP-0.5 (~100 mAh g^{-1}) is much higher than the theoretical value, indicating potential multi-redox reactions in the electrode. However, at a high content of Cr^{3+} in NVCP-1.0, the reduced V element and increased carbon content lead to a specific capacity decrease, which is consistent with the reported result.[44] To verify the specific cation intercalation behaviors, NVP and NVCP-0.5 were systematically tested in 2 *m* $ZnOTF_2$

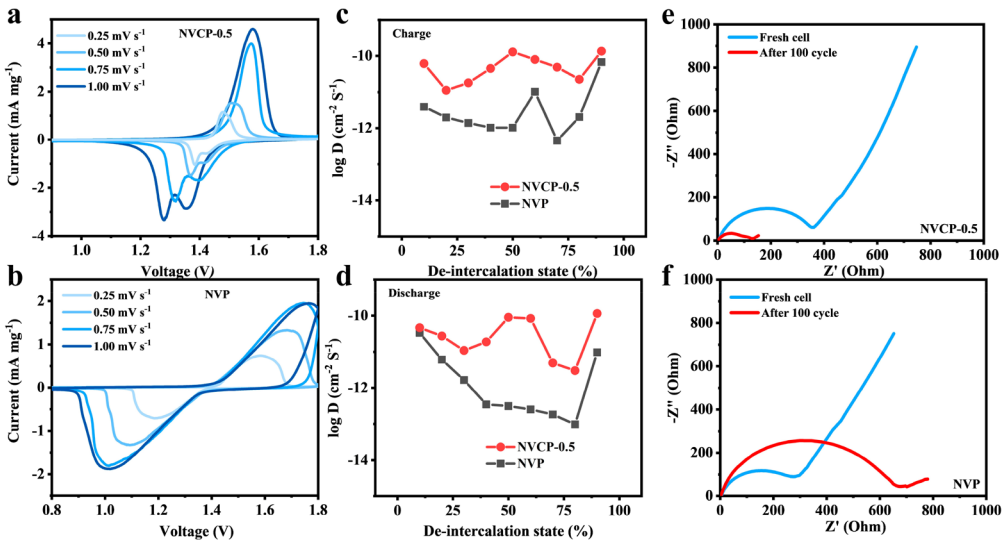

Figure 2. Electrochemical kinetic analysis. CV curves of the (a) Zn/NVCP-0.5 and (b) Zn/NVP cells at various scan rates. (c, d) The corresponding ions diffusion coefficients of NVP and NVCP-0.5 electrodes from GITT results. (e, f) Nyquist plots of the Zn/NVCP-0.5 and Zn/NVP cells before and after cycling.

+ 1 *m* NaOTF, 2 *m* $ZnOTF_2$, and 1 *m* NaOTF aqueous electrolytes, and the initial GCD profiles at 50 mA g^{-1} are displayed in Figure S11. The Cr-doped NVCP-0.5 electrode has higher capacity for single Na^+ (19.8 mAh g^{-1}), single Zn^{2+} (65.3 mAh g^{-1}), and Na^+/Zn^{2+} (99.6 mAh g^{-1}) intercalation than the NVP (11.8, 56.0, and 85.4 mAh g^{-1}, respectively), indicating the predominant Zn^{2+} intercalation of the NVP-based materials in AZBs.

The rate performance of the $Na_3V_{2-x}Cr_x(PO_4)_3$ materials was evaluated, as shown in Figure 1b. It can be seen that the NVCP-0.5 electrode has higher reversible capacities of 102, 101, 97, 91, and 84 mAh g^{-1} at current densities of 50, 100, 250, 500, and 1000 mA g^{-1}, respectively, which are substantially higher than those of NVP and NVCP-1.0. When the current goes back to 100 mA g^{-1}, a capacity comparable to the initial specific capacity value is almost entirely recovered. Note that although NVCP-1.0 exhibits low specific capacities, the rate capability is much enhanced, with a capacity retention of 85% at 1000 mA g^{-1} of that at 50 mA g^{-1}. The selected GCD profiles are presented in Figure 1c and Figure S12, clearly illustrating the reduced voltage polarizations in NVCP-based electrodes. These results suggest that the Cr substitution can efficiently improve the rate capability and reversibility of NVP in AZBs.

It is critical to evaluate the low-rate cycling stability of V-based cathodes in aqueous batteries, as the operational currents required by a storage device for the power grid are around 0.5−2 C and do not exceed 10 C.[45] In this context, cycling stability tests of the NVP, NVCP-0.5, and NVCP-1.0 electrodes were performed at a current density of 50 mA g^{-1} (~0.5 C), as shown in Figure 1d. The reversible capacity of NVCP-0.5 is stabilized at 94 mAh g^{-1}, with an average CE of 99.7% and a capacity retention of 92% after 300 cycles at a low current density of 50 mA g^{-1} However, the NVP electrode only achieves 30% capacity after 270 cycles. In addition, the Cr-doped NVCP species also exhibit excellent long-term cycling stability at high rate. Figure 1e demonstrates the long-term cycling results at a relatively high current density of 1000 mA g^{-1} for NVP, NVCP-0.5, and NVCP-1.0 electrodes. Impressively, compared with the fast capacity fade of NVP, NVCP-0.5 behaves at a prospective specific capacity of ~58 mAh g^{-1} after extra-long cycling up to 10,000 cycles (~68.3% capacity retention), with a high average CE of 99.99%. The specific capacities of NVP and NVCP-0.5 compounds, based on the mass deducting the carbon percentages in the composites (Figure S13), further verifies the superior performance of the NVCP-0.5 electrode. To prove the robustness of the as-prepared NVCP-0.5 materials, four additional cells were tested at low and high current densities, as shown in Figures S14 and S15. All these identical cells exhibit consistent performance, demonstrating the high reproducibility of the electrochemical properties. Moreover, the cycling performance of the NVCP-1.0 material is also improved, in spite of the low specific capacities. Besides, the average working voltage of NVCP-0.5 electrode is 1.4 V, resulting in a specific energy density of ~140 Wh kg^{-1} calculated based on eq (1) in the Supporting Information. Such performance authenticates that the introduction of Cr^{3+} can improve the cycling stability and energy density of NVP-based cathodes and is of great promise among the various advanced NVP-based cathodes for AZBs (Table S7).

To understand the redox mechanisms between the NVP and Cr-doped NVP cathode materials, cyclic voltammetry (CV) tests were performed at various scan rates in AZBs. In Figure 2a, two couples of stepwise redox peaks are detected in the NVCP-0.5 electrode at a low scan rate, indicating the potential multi-redox reactions. Specifically, during the initial anodic scan at 0.25 mV s^{-1}, two oxidation peaks located at 1.47 and 1.49 V can be observed, and accordingly more distinct reduction peaks at 1.42 and 1.38 V appeared during the subsequent cathodic scan. When the scanning rate was increased, the gap between oxidation peaks and reduction peaks widened, which can be attributed to the polarization and is also consistent with the GCD profile (Figure 1a). It has already been reported that the quasi-two-stage Zn^{2+}/Na^+ intercalation in NVP material also exhibits two redox peaks, while the subsequent Zn^{2+} intercalation takes place at lower voltage (~1.1 V).[21,43] In contrast, the NVP electrode (Figure 2b) displays only a couple of broad redox peaks and severe voltage polarization at different scan rates, implying limited

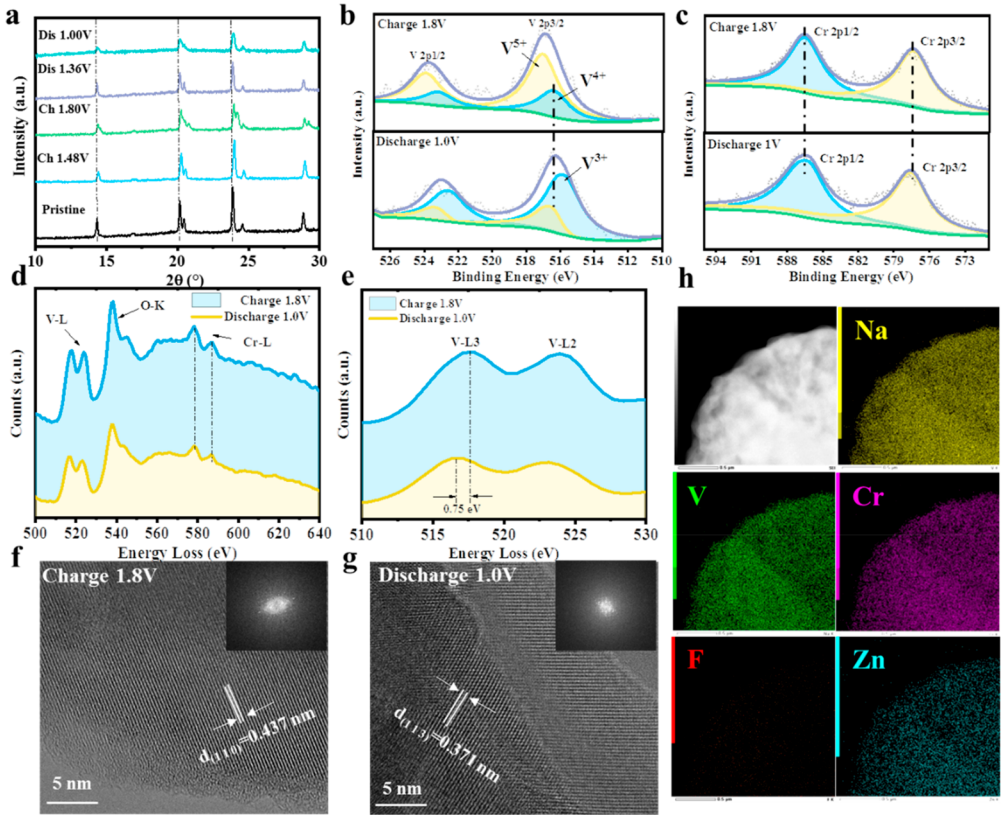

Figure 3. Post-mortem analysis of the cycled NVCP-0.5 electrodes. (a) Amplified *ex situ* XRD patterns at the initial cycle. (b, c) V 2p and Cr 2p high-resolution XPS spectra. (d) EELS spectra recorded from the surface to the bulk electrode. (e) V-$L_{2,3}$ EELS spectra, where L_3 and L_2 represent excitations of $2p^{3/2} \rightarrow 3d$ and $2p^{1/2} \rightarrow 3d$, respectively. (f, g) HR-TEM images recorded at charge and discharge states after 5 cycles. (h) Energy-dispersive X-ray spectroscopy (EDX) elemental mapping in STEM mode at 1.0 V discharge.

electrochemical activity. In order to more intuitively represent the redox reactions in the electrochemical reaction of NVCP electrode, differential capacity vs potential (dQ/dV) curves of NVCP-0.5 and NVP derived from the GCD results at 500 mA g^{-1} are displayed in Figure S16. Differential capacity is defined as the relative change in capacity (ΔQ) over the corresponding voltage range (ΔV), and the peaks of the differential capacity curves (dQ/dV) represent phase equilibria.[46] The NVCP-0.5 electrode shows two each anodic and cathodic peaks at different voltages, suggesting a two-stage redox reaction. In contrast, only each one anodic and cathodic peaks were observed for NVP electrode, in agreement with the CV results. Thus, the two-stage redox reactions at higher voltages in the NVCP electrode can be ascribed to the successive multi-electron redox reactions. Figure S17 presents the relationships between the peak current (i) and the square root of scan rate ($v^{1/2}$) in log scale (see detailed calculation in Supporting Information) to clarify the capacity contribution type for Zn-ion storage in NVP and NVCP-0.5 cathodes. According to eq (2) in the Supporting Information, a b value of 0.5 implies a diffusion mechanism, while a b value of 1.0 indicates the predominant capacitive behavior. For the NVCP-0.5 material, the b values of the cathodic and anodic peaks were calculated to be 0.91, 0.85, and 0.82, respectively, indicating the facilitated capacitive contribution and combined diffusion reaction in NVCP-0.5 material. However, the b values of the NVP electrode are smaller than those of the NVCP, illustrating the lower capacitive contribution. According to eq (3) in the Supporting Information, k_1v and $k_2v^{1/2}$ represent the capacitive and diffusion-controlled contributions, respectively. As displayed in Figure S18, 59.1% of the total capacity is identified as the capacitive contribution in the NVCP-0.5 electrode at 0.5 mV s^{-1}, which is higher than that of NVP (44.3%), implying the enhanced capacitive behavior with fast reaction kinetics in the NVCP-0.5.

The galvanostatic intermittent titration technique (GITT) was employed to investigate the cation diffusion dynamics in the electrodes. The results are shown in Figure S19. As depicted in Figure 2c,d, the apparent cation diffusion coefficients in the NVP and NVCP-0.5 electrodes during (de)intercalation processes were calculated. It is expected that the diffusion coefficients of the NVCP electrode are about an order of magnitude higher than those of the NVP, which supports the statement that Cr substitution is beneficial for enhancing the high-rate performance. Meanwhile, electrochemical impedance spectroscopy (EIS) experiments were adopted to understand the charge-transfer behaviors and ion diffusion kinetics, and the results are displayed in Figure 2e,f. The collected Nyquist plot of the Zn/NVP cell before and after 100 cycles reveals an increase of charge-transfer resistance after cycling, which is typically caused by the dissolution of V-based species and will result in poor cycling stability.[18] However, the NVCP-0.5-based cell exhibits an observably decreased charge-transfer resistance with much lower values, implying its favorable kinetic properties. These observations well explain the superior electrochemical performance of the NVCP-0.5 cathode.

In order to understand the redox reaction mechanism in the NVCP-0.5 electrode, *ex situ* XRD and XPS characterizations were conducted. The recorded *ex situ* XRD patterns on the

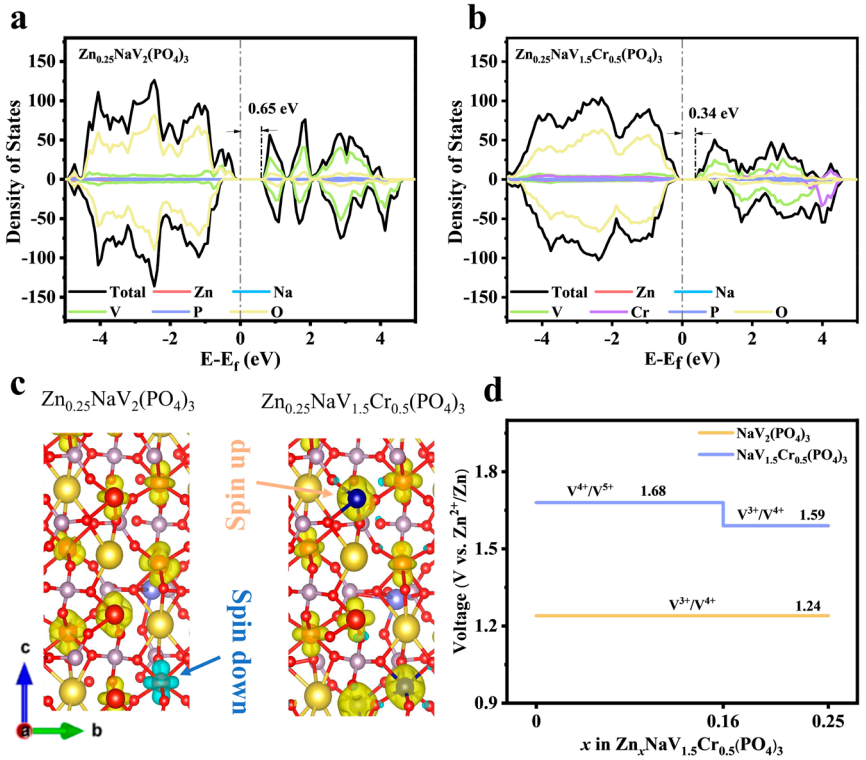

Figure 4. Density functional theory (DFT) calculations. Calculated density of states (DOS) and the corresponding partial density of states (PDOS) diagrams of (a) $Zn_{0.25}NaV_{1.5}Cr_{0.5}(PO_4)_3$ and (b) $Zn_{0.25}NaV_2(PO_4)_3$. (c) Comparison of the electronic spin states for these two samples. (d) Calculated voltage profiles for $Zn_xV_{1.5}Cr_{0.5}(PO_4)_3$ and $Zn_xV_{1.5}Cr_{0.5(}PO_4)_3$ (x = 0, 0.16, 0.25).

NVCP-0.5 electrode during the initial discharge and charge processes are shown in Figure S20. As can be seen in the amplified XRD patterns (Figure 3a), all the dominant diffraction peaks shifted to a higher 2θ degree along with the initial charging procedure to 1.8 V, due to the extraction of Na^+ from the NVP structure causing lattice structure contraction. At a charged state of 1.8 V, new diffraction peaks at 20.8° and 29.2° occur which can be indexed to the Na-deficient $NaV_2(PO_4)_3$ phase.[27] Upon discharging, the corresponding diffraction peaks gradually tuned back to lower 2θ degrees without impurity peaks, while the final 2θ degree value of these peaks is a little bit higher than those of the pristine NVCP-0.5 electrode, suggesting the occupancy for Zn^{2+} with low ionic radius into the empty 18e sites of the lattice.[43] The *ex situ* XRD characterization gives a feasible sodium-ion extraction/Zn-ion insertion mechanism with the maintenance of the general NASICON framework during the first charge/discharge process.

The Rietveld-refined XRD patterns of the cycled electrodes at charging and discharging states (Figure S21) allow for a more descriptive analysis of the structural changes associated with the (de)intercalation process. The refined V and Cr occupancies obtained from the powder XRD refinement were used as models for the *ex situ* XRD refinements. The lattice parameters and occupancy values are listed in Tables S8, S9, and S10. After charging to 1.8 V, two phases coexist in the diffraction pattern, corresponding to $Na_3V_{1.5}Cr_{0.5}(PO_4)_3$ and $NaV_{1.5}Cr_{0.5}(PO_4)_3$. The 6b site for Na1 is still occupied, with Na2 fully unoccupied. The Na^+-extracted NVCP phase yields the high phase fraction of 90%, while pristine $Na_3V_{1.5}Cr_{0.5}(PO_4)_3$ remains at 10%. The lattice parameter values change to $a = b = 8.62$ Å and $c = 21.57$ Å, resulting in a significant lattice shrinkage with a unit cell volume of 1388.6 $Å^3$. This corresponds to a contraction of the crystal structure after extraction of Na^+, with the unit cell volume decreasing by ~3.0%, which is half less than that of the reported conventional NVP after charging.[43]

When discharged to 1.0 V, the lattice parameters and unit cell volume (Table S8) are $a = b = 8.77$ Å, $c = 21.96$ Å, and $V = 1462.5$ $Å^3$, indicating lattice expansion after Zn^{2+} insertion. Because a maximum of 2 mol of Zn^{2+} (or Na^+) can be present in the 18e site, the Zn mole fraction based on the Zn occupancy of 0.125 was calculated to be 0.25 [i.e., $Zn_{0.25}NaV_2(PO_4)_3$].[43] In this context, the Zn^{2+}-inserted phase of $Zn_{0.25}NaV_{1.5}Cr_{0.5}(PO_4)_3$ was considered as the third phase for the refinement. With these simulated phases, the Rietveld-refined weighed residual factor (R_{wp}) was 4.49, thus providing confidence in this simulation. The results indicate that the lattice accommodates Zn^{2+} into the empty 18e sites with an occupancy of 0.125 and Na remains in the 6b site at full occupancy. Upon discharging, the phase fraction of $Zn_{0.25}NaV_{1.5}Cr_{0.5}(PO_4)_3$ was ~89.8%, while the Na^+-extracted phase ($NaV_{1.5}Cr_{0.5}(PO_4)_3$) shows a low fraction of only 0.2%. The Na^+-inserted NVCP phase remains at 9.9%, indicating that the Zn^{2+} insertion at the 18e sites is the main electrochemical reaction.

To track the valence change involving the redox reactions, *ex situ* XPS spectra were collected on the cycled electrodes. The full XPS survey spectra of the cycled NVCP-0.5 electrodes are presented in Figure S22a,b, which clearly demonstrate presence of Na, F, Cr, and V elements in the charged electrode, while additional strong peaks related to Zn are observed in the discharged one (Figure S22c). It should be noted that very weak peak intensity of the Na 1s peak was

detected in both the charged and discharged electrodes (Figure S22d), indicating the limited amount Na^+ involved in the intercalation reaction. This observation suggests the successful intercalation of Zn in the NVCP cathode after discharging. Figure 3b,c shows the high-resolution V 2p and Cr 2p XPS spectra recorded at charge (1.8 V) and discharge (1.0 V) states, respectively. At charged state, the characteristic V 2p peak can be deconvoluted into two peaks, implying the existence of V^{5+} (V $2p_{3/2}$: 517.1 eV) and V^{4+} (V $2p_{3/2}$: 516.5 eV). When the cell is discharged to the low voltage of 1.0 V, the V 2p peaks shift to lower binding energy and can be deconvoluted into V^{4+} (V $2p_{3/2}$: 516.5 eV) and V^{3+} (V $2p_{3/2}$: 515.8 eV), indicating the V transition metal element undergoes multi-electron reactions from V^{3+} to V^{5+} during cation intercalation.[47,48] In contrast, the binding energies of Cr $2p_{3/2}$ and Cr $2p_{1/2}$ keep unchanged during the charge and discharge process (Figure 3c), suggesting that the Cr dopant may not participate in the redox reactions in the specific voltage range of 1.0−1.8 V for the aqueous cell cycling. In addition, electron energy loss spectroscopy (EELS) was also employed to further determine the valence change in the bulk electrodes during the redox reactions. The selected areas for collecting EELS spectra are shown in Figure S23. From Figure 3d, it can be seen that the Cr $L_{2,3}$ edge of the charged NVCP-0.5 electrode is located at 577.5 eV, and there is no shift at the discharged state. This result confirms that the Cr has no change in valence and does not participate in the redox reaction, consistent with the XPS results. In contrast, the V $L_{2,3}$ edge (Figure 3e) shifts from 517.5 eV at charge 1.8 V to 516.75 eV at discharge 1.0 V, verifying the reduction of V to a lower valence state after cation intercalation.[49,50]

HR-TEM images were collected at charge (1.8 V) and discharge (1.0 V) states after 5 cycles to provides further proof for the structure stability of NVCP-0.5 cathodes in AZBs (Figure 3f,g). Both the distinctive lattice fringes in the cycled electrodes, which refer well to the (110) plane and the (113) plane of the $NaV_{1.5}Cr_{0.5}(PO_4)_3$ and $Zn_xNaV_{1.5}Cr_{0.5}(PO_4)_3$ phases with *d*-spacings of 0.437 and 0.371 nm, and their selected-area electron diffraction (SAED) patterns manifest their stable crystal structure for cation (de)intercalation reactions. The STEM-EDX mapping results on the discharged NVCP-0.5 electrode underscore the homogeneous elemental distribution of V, F, Na Cr, and Zn, verifying the Zn^{2+} intercalation, as shown in Figure 3h. On the basis of the above experimental results, it is fully evidenced that the Cr^{3+} dopant can successfully activate the multi-electron reactions of V^{3+}/V^{5+} redox couples in the NASICON structure as well as trigger reversible two-phase and solid-solution reactions, accounting for the improvement of their electrochemical performance as cathodes for AZBs.

To theoretically unfold the superior kinetics and dynamics of $Na_3V_{1.5}Cr_{0.5}(PO_4)_3$ for Zn^{2+} storage, optimized models of $Zn_{0.25}NaV_{1.5}Cr_{0.5}(PO_4)_3$ and $Zn_{0.25}NaV_2(PO_4)_3$ (Figure S24) were built for the density functional theory (DFT) calculations. The density of states (DOS) and the corresponding partial density of states (PDOS) diagrams were calculated as shown in Figure 4a,b. The valence bands for both samples consist of the hybridized V 3d, P 2p, Na 3s, Zn 2p, and O 1p orbitals, and the Cr 3d orbital is also observed in $Zn_{0.25}NaV_{1.5}Cr_{0.5}(PO_4)_3$. Owing to the hybridized Cr 3d orbitals, the forbidden band gap of $Zn_{0.25}NaV_{1.5}Cr_{0.5}(PO_4)_3$ is reduced to 0.34 eV, lower than that of $Zn_{0.25}NaV_2(PO_4)_3$ (0.65 eV), demonstrating that the Cr^{3+} substitution can induce to the enhanced electron conduction and Zn^{2+} transport, which can be beneficial for the activation of the high-voltage redox couple of V^{4+}/V^{5+} in $Zn_{0.25}NaV_{1.5}Cr_{0.5}(PO_4)_3$. In addition, the electronic spin state comparison extracted from DFT calculation results (Figure 4c) further indicates that the unpaired electron of Cr^{3+} ions in $Zn_{0.25}NaV_{1.5}Cr_{0.5}(PO_4)_3$ results in the variation of spin magnetic moment in the 3d orbitals of VO_6 and CrO_6 octahedra, which activates the last remaining valence electron to enable access to the high-voltage redox couple V^{4+}/V^{5+}. Moreover, calculated using the equation $E_{form} = {}^1/_3[E(Zn_{0.25}NaV_{1-x}Cr_x(PO_4)_3) - E(NaV_{1-x}Cr_x(PO_4)_3) - 3E(Zn)]$, the formation energies of these two samples are illustrated in Table S11; the formation energy of $Zn_{0.25}NaV_{1.5}Cr_{0.5}(PO_4)_3$ is −3.30 eV, which is more negative than that of $Zn_{0.25}NaV_2(PO_4)_3$ (−2.49 eV). This implies that $Zn_{0.25}NaV_{1.5}Cr_{0.5}(PO_4)_3$ is the more thermodynamically stable phase, and both of these phases can be electrochemically achieved, which can further explain the multi-electron reaction nature in the Cr-doped NASCION-type material. From the lowest-energy structure, the optimized lowest-energy meso-phase of $Zn_{0.16}NaV_{1.5}Cr_{0.5}(PO_4)_3$ was established to calculate the theoretical voltage profile of $NaV_{1.5}Cr_{0.5}(PO_4)_3$ during the insertion/extraction of Zn^{2+} ions. As shown in Figure 4d, the sequential reactions based on the intermediate phase (i.e., from $NaV_{1.5}Cr_{0.5}(PO_4)_3$ to $Zn_{0.16}NaV_{1.5}Cr_{0.5}(PO_4)_3$, and from $Zn_{0.16}NaV_{1.5}Cr_{0.5}(PO_4)_3$ to $Zn_{0.25}NaV_{1.5}Cr_{0.5}(PO_4)_3$) are predicted to occur at 1.68 V for V^{4+}/V^{5+} and 1.59 V for V^{3+}/V^{4+}, while the undoped phase $NaV_2(PO_4)_3$ exhibits only one reaction, at 1.24 V for V^{3+}/V^{4+}—these are close to the experimental values. These results indicate that the decreased forbidden band gap resulting from Cr substitution and the unpaired 3d orbital electrons in Cr^{3+}, which is electrochemically inactive, have strong influences on the activation of the high-voltage V^{4+}/V^{5+} redox reaction in NASICON-type materials for Zn^{2+} storage capability.

In summary, we delicately investigated the electrochemical and structural properties of the NASICON-type materials $Na_3V_{2-x}Cr_x(PO_4)_3$ as cathodes in AZBs. Benefiting from the incorporation of Cr^{3+}, significant improvements in both the high-rate capacity and long-term cycling stability have been achieved. As an example, the $Na_3V_{1.5}Cr_{0.5}(PO_4)_3$ (NVCP-0.5) material delivers a high reversible capacity of 84.4 mAh g^{-1} at a high current density of 1000 mA g^{-1} with ultrahigh cycling stability (68% capacity retention after extra-long cycling up to 10,000 cycles). By using post-mortem analysis, the role of Cr^{3+} dopant in the activation of multi-electron reactions based on V^{3+}/V^{5+} redox couples in the NASICON structure has been revealed, involving reversible two-phase and solid-solution transitions. Furthermore, DFT calculation results disclosed that Cr doping can contribute to the decreased forbidden band gap and improved Zn^{2+} transport capability in the robust structure, enabling access to the muti-electron reaction at high voltage. This work provides a guiding significance for designing advanced NASICON-type cathode materials with a multi-electron reaction mechanism for high-energy and durable aqueous zinc batteries.

ASSOCIATED CONTENT

Data Availability Statement

The data that support the findings of this study are available from the corresponding author upon reasonable request.

AUTHOR INFORMATION

Corresponding Authors

Stefano Passerini − *Helmholtz Institute Ulm (HIU), D-89081 Ulm, Germany; Karlsruhe Institute of Technology (KIT), D-76021 Karlsruhe, Germany;* orcid.org/0000-0002-6606-5304; Email: stefano.passerini@kit.edu

Huang Zhang − *Institute of Flexible Electronics, Northwestern Polytechnical University, Xi'an 710072, China;* orcid.org/0000-0002-7695-261X; Email: iamhzhang@nwpu.edu.cn

Authors

Kaidi Wang − *Institute of Flexible Electronics, Northwestern Polytechnical University, Xi'an 710072, China*

Huihua Li − *Helmholtz Institute Ulm (HIU), D-89081 Ulm, Germany; Karlsruhe Institute of Technology (KIT), D-76021 Karlsruhe, Germany*

Gaoli Guo − *Institute of Flexible Electronics, Northwestern Polytechnical University, Xi'an 710072, China*

Leilei Zheng − *Institute of Flexible Electronics, Northwestern Polytechnical University, Xi'an 710072, China*

Author Contributions

H.Z. and S.P. supervised the work. K.W. and H.Z. wrote the draft of the manuscript. K.W., H.L., and G.G. carried out the material synthesis, cell fabrication, and characterizations. L.Z. performed the material characterization. All authors discussed the results and contributed to the final manuscript.

Notes

The authors declare no competing financial interest.

ACKNOWLEDGMENTS

This work was financially supported by the Guangdong Basic and Applied Basic Research Foundation (2020A1515110587), the Ningbo Natural Science Foundation (202003N4055), the Natural Science Basic Research Program of Shaanxi (2021JQ-110), the Fundamental Research Funds for the Central Universities, and the Helmholtz Association within the Network of Excellence on post-lithium batteries (ExNet-0035).

REFERENCES

(1) Xu, C.; Li, B.; Du, H.; Kang, F. Energetic Zinc Ion Chemistry: The Rechargeable Zinc Ion Battery. *Angew. Chem., Int. Ed.* **2012**, *51* (4), 933−935.

(2) Kittner, N.; Lill, F.; Kammen, D. M. Energy storage deployment and innovation for the clean energy transition. *Nat. Energy* **2017**, *2* (9), 17125.

(3) Dunn, B.; Kamath, H.; Tarascon, J.-M. Electrical Energy Storage for the Grid: A Battery of Choices. *Science* **2011**, *334* (6058), 928−935.

(4) Zhang, L.; Chen, L.; Zhou, X.; Liu, Z. Towards High-Voltage Aqueous Metal-Ion Batteries Beyond 1.5 V: The Zinc/Zinc Hexacyanoferrate System. *Adv. Energy Mater.* **2015**, *5* (2), 1400930.

(5) Zhang, H.; Liu, X.; Li, H.; Hasa, I.; Passerini, S. Challenges and Strategies for High-Energy Aqueous Electrolyte Rechargeable Batteries. *Angew. Chem., Int. Ed.* **2021**, *60* (2), 598−616.

(6) Chao, D.; Zhou, W.; Xie, F.; Ye, C.; Li, H.; Jaroniec, M.; Qiao, S.-Z. Roadmap for advanced aqueous batteries: From design of materials to applications. *Sci. Adv.* **2020**, *6* (21), eaba4098.

(7) Fang, G.; Zhou, J.; Pan, A.; Liang, S. Recent Advances in Aqueous Zinc-Ion Batteries. *ACS Energy Lett.* **2018**, *3* (10), 2480−2501.

(8) Konarov, A.; Voronina, N.; Jo, J. H.; Bakenov, Z.; Sun, Y.-K.; Myung, S.-T. Present and Future Perspective on Electrode Materials for Rechargeable Zinc-Ion Batteries. *ACS Energy Lett.* **2018**, *3* (10), 2620−2640.

(9) Kundu, D.; Adams, B. D.; Duffort, V.; Vajargah, S. H.; Nazar, L. F. A high-capacity and long-life aqueous rechargeable zinc battery using a metal oxide intercalation cathode. *Nat. Energy* **2016**, *1* (10), 16119.

(10) Zhang, N.; Dong, Y.; Jia, M.; Bian, X.; Wang, Y.; Qiu, M.; Xu, J.; Liu, Y.; Jiao, L.; Cheng, F. Rechargeable Aqueous Zn−V_2O_5 Battery with High Energy Density and Long Cycle Life. *ACS Energy Lett.* **2018**, *3* (6), 1366−1372.

(11) Zhong, C.; Liu, B.; Ding, J.; Liu, X.; Zhong, Y.; Li, Y.; Sun, C.; Han, X.; Deng, Y.; Zhao, N.; Hu, W. Decoupling electrolytes towards stable and high-energy rechargeable aqueous zinc−manganese dioxide batteries. *Nat. Energy* **2020**, *5* (0), 440−449.

(12) Zeng, X.; Liu, J.; Mao, J.; Hao, J.; Wang, Z.; Zhou, S.; Ling, C. D.; Guo, Z. Toward a Reversible Mn^{4+}/Mn^{2+} Redox Reaction and Dendrite-Free Zn Anode in Near-Neutral Aqueous Zn/MnO2 Batteries via Salt Anion Chemistry. *Adv. Energy Mater.* **2020**, *10* (32), 1904163.

(13) Li, H.; Xu, M.; Zhang, Z.; Lai, Y.; Ma, J. Engineering of Polyanion Type Cathode Materials for Sodium-Ion Batteries: Toward Higher Energy/Power Density. *Adv. Funct. Mater.* **2020**, *30* (28), 2000473.

(14) Zhang, K.-Y.; Gu, Z.-Y.; Ang, E. H.; Guo, J.-Z.; Wang, X.-T.; Wang, Y.; Wu, X.-L. Advanced polyanionic electrode materials for potassium-ion batteries: Progresses, challenges and application prospects. *Mater. Today* **2022**, *54*, 189−201.

(15) Liu, Y.; Li, W.; Xia, Y. Recent Progress in Polyanionic Anode Materials for Li (Na)-Ion Batteries. *Electrochem. Energy Rev.* **2021**, *4* (3), 447−472.

(16) Chen, S.; Wu, C.; Shen, L.; Zhu, C.; Huang, Y.; Xi, K.; Maier, J.; Yu, Y. Challenges and Perspectives for NASICON-Type Electrode Materials for Advanced Sodium-Ion Batteries. *Adv. Mater.* **2017**, *29* (48), 1700431.

(17) Li, H.; Jin, T.; Chen, X.; Lai, Y.; Zhang, Z.; Bao, W.; Jiao, L. Rational Architecture Design Enables Superior Na Storage in Greener NASICON-$Na_4MnV(PO_4)_3$ Cathode. *Adv. Energy Mater.* **2018**, *8* (24), 1801418.

(18) Zhang, H.; Tan, X.; Li, H.; Passerini, S.; Huang, W. Assessment and progress of polyanionic cathodes in aqueous sodium batteries. *Energy Environ. Sci.* **2021**, *14* (11), 5788−5800.

(19) Chen, G.; Huang, Q.; Wu, T.; Lu, L. Polyanion Sodium Vanadium Phosphate for Next Generation of Sodium-Ion Batteries—A Review. *Adv. Funct. Mater.* **2020**, *30* (34), 2001289.

(20) Zhang, H.; Qin, B.; Han, J.; Passerini, S. Aqueous/Nonaqueous Hybrid Electrolyte for Sodium-Ion Batteries. *ACS Energy Lett.* **2018**, *3* (7), 1769−1770.
(21) Hu, P.; Zhu, T.; Wang, X.; Zhou, X.; Wei, X.; Yao, X.; Luo, W.; Shi, C.; Owusu, K. A.; Zhou, L.; Mai, L. Aqueous Zn//$Zn(CF_3SO_3)_2$//$Na_3V_2(PO_4)_3$ Batteries with Simultaneous Zn^{2+}/Na^+ Intercalation /De-intercalation. *Nano Energy* **2019**, *58*, 492−498.
(22) Hu, P.; Zou, Z.; Sun, X.; Wang, D.; Ma, J.; Kong, Q.; Xiao, D.; Gu, L.; Zhou, X.; Zhao, J.; Dong, S.; He, B.; Avdeev, M.; Shi, S.; Cui, G.; Chen, L. Uncovering the Potential of M1-Site-Activated NASICON Cathodes for Zn-Ion Batteries. *Adv. Mater.* **2020**, *32* (14), 1907526.
(23) Li, G.; Yang, Z.; Jiang, Y.; Jin, C.; Huang, W.; Ding, X.; Huang, Y. Towards polyvalent ion batteries: A zinc-ion battery based on NASICON structured $Na_3V_2(PO_4)_3$. *Nano Energy* **2016**, *25*, 211−217.
(24) Liu, C.; Xie, X.; Lu, B.; Zhou, J.; Liang, S. Electrolyte Strategies toward Better Zinc-Ion Batteries. *ACS Energy Lett.* **2021**, *6* (3), 1015−1033.
(25) Lin, X.; Zhou, G.; Liu, J.; Robson, M. J.; Yu, J.; Wang, Y.; Zhang, Z.; Kwok, S. C. T.; Ciucci, F. Bifunctional Hydrated Gel Electrolyte for Long-Cycling Zn-Ion Battery with NASICON-Type Cathode. *Adv. Funct. Mater.* **2021**, *31* (42), 2105717.
(26) Zeng, X.; Mao, J.; Hao, J.; Liu, J.; Liu, S.; Wang, Z.; Wang, Y.; Zhang, S.; Zheng, T.; Liu, J.; Rao, P.; Guo, Z. Electrolyte Design for In Situ Construction of Highly Zn^{2+}-Conductive Solid Electrolyte Interphase to Enable High-Performance Aqueous Zn-Ion Batteries under Practical Conditions. *Adv. Mater.* **2021**, *33* (11), 2007416.
(27) Guo, G.; Tan, X.; Wang, K.; Zhang, H. High-Efficiency and Stable Zn-$Na_3V_2(PO_4)_3$ Aqueous Battery Enabled by Electrolyte-Induced Interphasial Engineering. *ChemSusChem* **2022**, *15* (11), e202200313.
(28) Aragón, M. J.; Lavela, P.; Ortiz, G. F.; Tirado, J. L. Benefits of Chromium Substitution in $Na_3V_2(PO_4)_3$ as a Potential Candidate for Sodium-Ion Batteries. *ChemElectroChem.* **2015**, *2* (7), 995−1002.
(29) Park, S.; Chotard, J.-N.; Carlier, D.; Moog, I.; Duttine, M.; Fauth, F.; Iadecola, A.; Croguennec, L.; Masquelier, C. An Asymmetric Sodium Extraction/Insertion Mechanism for the Fe/V-Mixed NASICON $Na_4FeV(PO_4)_3$. *Chem. Mater.* **2022**, *34* (9), 4142−4152.
(30) Xu, C.; Zhao, J.; Wang, Y.-A.; Hua, W.; Fu, Q.; Liang, X.; Rong, X.; Zhang, Q.; Guo, X.; Yang, C.; Liu, H.; Zhong, B.; Hu, Y.-S. Reversible Activation of $V^{4+/V5+}$ Redox Couples in NASICON Phosphate Cathodes. *Adv. Energy Mater.* **2022**, *12* (25), 2200966.
(31) Li, H.; Jin, T.; Chen, X.; Lai, Y.; Zhang, Z.; Bao, W.; Jiao, L. Rational Architecture Design Enables Superior Na Storage in Greener NASICON-$Na_4MnV(PO_4)_3$ Cathode. *Adv. Energy Mater.* **2018**, *8* (24), 1801418.
(32) Criado, A.; Lavela, P.; Tirado, J. L.; Pérez-Vicente, C. Increasing Energy Density with Capacity Preservation by Aluminum Substitution in Sodium Vanadium Phosphate. *ACS Appl. Mater. Interfaces* **2020**, *12* (19), 21651−21660.
(33) Sun, C.; Zhao, Y.; Ni, Q.; Sun, Z.; Yuan, X.; Li, J.; Jin, H. Reversible multielectron redox in NASICON cathode with high energy density for low-temperature sodium-ion batteries. *Energy Storage Mater.* **2022**, *49*, 291−298.
(34) Wu, Z.; Ye, F.; Liu, Q.; Pang, R.; Liu, Y.; Jiang, L.; Tang, Z.; Hu, L. Simultaneous Incorporation of V and Mn Element into Polyanionic NASICON for High Energy-Density and Long-Lifespan Zn-Ion Storage. *Adv. Energy Mater.* **2022**, *12* (23), 2200654.
(35) Chen, M.; Hua, W.; Xiao, J.; Zhang, J.; Lau, V. W.-h.; Park, M.; Lee, G.-H.; Lee, S.; Wang, W.; Peng, J.; Fang, L.; Zhou, L.; Chang, C.-K.; Yamauchi, Y.; Chou, S.; Kang, Y.-M. Activating a Multielectron Reaction of NASICON-Structured Cathodes toward High Energy Density for Sodium-Ion Batteries. *J. Am. Chem. Soc.* **2021**, *143* (43), 18091−18102.
(36) Saravanan, K.; Mason, C. W.; Rudola, A.; Wong, K. H.; Balaya, P. The First Report on Excellent Cycling Stability and Superior Rate Capability of $Na_3V_2(PO_4)_3$ for Sodium Ion Batteries. *Adv. Energy Mater.* **2013**, *3* (4), 444−450.
(37) Goodenough, J. B.; Hong, H. Y. P.; Kafalas, J. A. Fast Na^+-ion transport in skeleton structures. *Mater. Res. Bull.* **1976**, *11* (2), 203−220.
(38) Cushing, B. L.; Goodenough, J. B. $Li_2NaV_2(PO_4)_3$: A 3.7 V Lithium-Insertion Cathode with the Rhombohedral NASICON Structure. *J. Solid State Chem.* **2001**, *162* (2), 176−181.
(39) Wang, M.; Tao, Y.; Zhang, D.; Sun, G.; Feng, P.; Chang, C. High rate and cyclic performance of $Na_{3-2x}Mg_xV_2(PO_4)_3$/C cathode for sodium-ion batteries. *J. Mater. Sci.: Mater. Electron.* **2020**, *31* (21), 18360−18369.
(40) Maurice, V.; Cadot, S.; Marcus, P. XPS, LEED and STM study of thin oxide films formed on Cr(110). *Surf. Sci.* **2000**, *458* (1), 195−215.
(41) Xu, Y.; Zhu, J.; Feng, J.; Wang, Y.; Wu, X.; Ma, P.; Zhang, X.; Wang, G.; Yan, X. A rechargeable aqueous zinc/sodium manganese oxides battery with robust performance enabled by Na_2SO_4 electrolyte additive. *Energy Storage Mater.* **2021**, *38*, 299−308.
(42) Wan, F.; Zhang, L.; Dai, X.; Wang, X.; Niu, Z.; Chen, J. Aqueous rechargeable zinc/sodium vanadate batteries with enhanced performance from simultaneous insertion of dual carriers. *Nat. Commun.* **2018**, *9* (1), 1656.
(43) Ko, J. S.; Paul, P. P.; Wan, G.; Seitzman, N.; DeBlock, R. H.; Dunn, B. S.; Toney, M. F.; Nelson Weker, J. NASICON $Na_3V_2(PO_4)_3$ Enables Quasi-Two-Stage Na^+ and Zn^{2+} Intercalation for Multivalent Zinc Batteries. *Chem. Mater.* **2020**, *32* (7), 3028−3035.
(44) Wang, Q.; Zhao, Y.; Gao, J.; Geng, H.; Li, J.; Jin, H. Triggering the Reversible Reaction of $V^{3+}/V^{4+}/V^{5+}$ in $Na_3V_2(PO_4)_3$ by Cr^{3+} Substitution. *ACS Appl. Mater. Interfaces* **2020**, *12* (45), 50315−50323.
(45) Zampardi, G.; La Mantia, F. Open challenges and good experimental practices in the research field of aqueous Zn-ion batteries. *Nat. Commun.* **2022**, *13* (1), 687.
(46) Bloom, I.; Jansen, A. N.; Abraham, D. P.; Knuth, J.; Jones, S. A.; Battaglia, V. S.; Henriksen, G. L. Differential voltage analyses of high-power, lithium-ion cells: 1. Technique and application. *J. Power Sources* **2005**, *139* (1), 295−303.
(47) Wang, J.; Wang, Y.; Seo, D.-H.; Shi, T.; Chen, S.; Tian, Y.; Kim, H.; Ceder, G. A High-Energy NASICON-Type Cathode Material for Na-Ion Batteries. *Adv. Energy Mater.* **2020**, *10* (10), 1903968.
(48) Zhao, Y.; Gao, X.; Gao, H.; Jin, H.; Goodenough, J. B. Three Electron Reversible Redox Reaction in Sodium Vanadium Chromium Phosphate as a High-Energy-Density Cathode for Sodium-Ion Batteries. *Adv. Funct. Mater.* **2020**, *30* (10), 1908680.
(49) Hosseini-Benhangi, P.; Garcia-Contreras, M. A.; Alfantazi, A.; Gyenge, E. L. Method for Enhancing the Bifunctional Activity and Durability of Oxygen Electrodes with Mixed Oxide Electrocatalysts: Potential Driven Intercalation of Potassium. *J. Electrochem. Soc.* **2015**, *162* (12), F1356−F1366.
(50) Chao, D.; Ye, C.; Xie, F.; Zhou, W.; Zhang, Q.; Gu, Q.; Davey, K.; Gu, L.; Qiao, S.-Z. Atomic Engineering Catalyzed MnO_2 Electrolysis Kinetics for a Hybrid Aqueous Battery with High Power and Energy Density. *Adv. Mater.* **2020**, *32* (25), 2001894.